Journal of ELECTRONIC MATERIALS, Vol. 48, No. 9, 2019
https://doi.org/10.1007/s11664-019-07345-w

Synthesis and Electrochemical Performances of $FeSe_2$/C as Anode Material for Lithium Ion Batteries

JIN BAI,[1] HUIMIN WU,[1] SHIQUAN WANG,[1] GUANGXUE ZHANG,[2,3]
and CHUANQI FENG[1,2,4]

1.—Hubei Collaborative Innovation Center for Advanced Organic Chemical Materials and Ministry of Education Key Laboratory for Synthesis and Applications of Organic Functional Molecules, Hubei University, Wuhan 430062, China. 2.—School of Nuclear Technology and Chemistry and Biology, Hubei University of Science and Technology, Xianning 437100, China. 3.—e-mail: zgx@hbust.edu.edu.cn. 4.—e-mail: cfeng@hubu.edu.cn

The Fe-based anode material for lithium ion batteries (LIBs) has gained great attention due to their abundant resources, high theoretical capacity and chemical stability. In this work, $FeSe_2$ and $FeSe_2$/C were synthesized by a simple hydrothermal method, and the samples were characterized by x-ray diffraction, scanning electron microscopy, thermogravimetric analysis, energy dispersive spectrometer and x-ray photoelectron spectrometer techniques, respectively. The electrochemical performances for both $FeSe_2$ and $FeSe_2$/C are tested as anode materials. These results exhibited that the $FeSe_2$/C composite has better electrochemical performance. $FeSe_2$/C composite has large specific capacities of 1060 mA h g^{-1} over 100 cycles at current density of 0.2 A g^{-1}. The rate performance of $FeSe_2$/C is also excellent. The capacity can be maintained at 697 mA h g^{-1} and 470 mA h g^{-1} at a current density of 3.0 A g^{-1} and 5.0 A g^{-1}. The excellent performance of $FeSe_2$/C composites makes it possible to be used as anode materials for LIB applications.

Key words: Chemical synthesis, inorganic compounds, electrochemical properties, anode material, lithium ion batteries

INTRODUCTION

With the progress of space technology and the demands of military equipment, a large amount of portable electronic products, and electric cars were researched and developed.[1–3] People's demand for batteries with the small size, high energy, reliability, and no pollution is more urgent. So the lithium ion battery as a type of high energy secondary battery has been developed rapidly. Nevertheless, the widely used anode material of LIBs, graphite, has a lower theoretical specific capacity (372 mA h g^{-1}) and poor rate capability.[4,5] Therefore, more anode materials need to be discovered to enhance the specific capacity and rate performance for LIBs.

In recent years, transition metal dichalcogenides (TMDs) were considered as the potential anode materials for LIBs due to their high theoretical capacities and good thermal stability. Some researches base on these materials (CoS_2, MoS_2 and FeS_2) had achieved an excellent electrochemical performance[6–9] and $FeSe_2$ has similar electrochemical properties as they have.[10] Besides, $FeSe_2$ possesses a high theoretical capacity of 501 mA h g^{-1}, which is higher than graphite. And an iron resource is rich in natural resources, low cost and environmentally friendly.[11–13] There are many attempts for $FeSe_2$ in other fields, e.g., solar cells,[14] semiconductors[15] and detecting visible radiation,[16] but there is little application in lithium ion batteries. Until recently, most effort has been concentrated on the formation of $FeSe_2$ films or low-dimensional micro/-nano-structures with little effort focused on the synthesis of $FeSe_2$ with three-dimensional structure like clusters.[17–20] This kind of structure cannot

---

(Received May 25, 2018; accepted June 1, 2019;

merely shorten the distance of ion diffusion, but also mitigate the self-aggregation of low-dimensional nanostructures.[21,22] Thus, it is a kind of potential material for LIBs.[23–25] Nevertheless, the proceeding of $FeSe_2$ anode material has been hindered by the poor conductivity and uncontrollable volume change during the cycling process, resulting in low capacity retention. To solve these issues, the compositing of $FeSe_2$ with carbon has been considered to be a viable strategy.[26,27] Furthermore, the introduction of carbon can also accelerate the electrons transfer and partly prevents the agglomeration of metal grains during the conversion reaction with Li.[28]

In this study, we synthesized $FeSe_2$/C clusters by an ordinary hydrothermal method, and used the $FeSe_2$/C composite as anode materials for LIBs. The $FeSe_2$/C composites exhibit higher specific capacity and better cycle performance than that of pure $FeSe_2$. The discharge capacity of $FeSe_2$ was 725 mA h g^{-1} after 100 cycles. Meanwhile, the discharge capacity of $FeSe_2$/C electrode reaches to 1060 mA h g^{-1}. When compared with the $MoSe_2$/C electrode (a specific capacity of 835 mA h g^{-1}),[29] the discharge capacity of the $FeSe_2$/C electrode still has a clear advantage. It indicates that $FeSe_2$/C is a promising anode material for lithium ion battery application.

EXPERIMENTAL PROCEDURES

Material Synthesis

In the process of synthesis, 1 mmol $(NH_4)_2Fe(SO_4)_2$ was dispersed in 20 ml of deionized water and stirred until completely dissolved at room temperature. Subsequently, 2 mmol SeO_2 and 12 ml hydrazine hydrate ($N_2H_4H_2O$) were successively added to the solution, magnetic stirring for 0.5 h. Then, 1 g glucose ($C_6H_{12}O_6$) was dissolved into the resulting mixture. Kept stirring for 2 h, the mixture solution was transferred into a 50 ml Teflon lined autoclave and with reaction at the temperature of 180°C for 6 h. The $FeSe_2$/C was obtained through centrifugation and washed three times with distilled water and ethanol, respectively. Finally, the $FeSe_2$/C was dried at 80°C for 12 h in vacuum. As a comparison, pure $FeSe_2$ was prepared in the same way without added glucose.

Characterization of the Samples

The morphologies and elemental analyses of the $FeSe_2$ and $FeSe_2$/C composites were characterized using an x-ray diffraction (XRD) with a Cu Kα radiation source. The materials microstructure was observed by scanning electron microscopy (SEM-JEOLJSM, 6510 V). The atomic composition of $FeSe_2$/C composites was detected by energy dispersive spectroscopy (EDS). The thermal behavior of $FeSe_2$/C composite was carried out by thermogravimetric analysis (TGA; DIAMOND) from 25°C to 900°C with a heating rate of 10°C min^{-1} and tested with air atmosphere. The valence states of the expected compounds were analyzed by an x-ray photoelectron spectrometer (XPS, Escalab 250Xi).

Electrochemical Performance

The electrochemical measurements of $FeSe_2$ and $FeSe_2$/C composites were measured through assembly into half-cells. The lithium metal was used as counter electrode and the working electrodes were consisting of active material, acetylene black, and poly (vinylidenefluoride) (PVDF) dispersed in *N*-methyl-2-pyrrolidene solution at a weight ratio of 60:30:10. The slurry was smeared evenly on the surface of copper foil and dried at 80°C in a vacuum oven for 10 h. The electrolyte was 1 M $LiPF_6$ in (1:1 by volume) ethylene carbonate/diethyl-carbonate (EC/DEC) and the celgard 2400 porous polypropylene was used as the separator. The coin cell was assembled in a glove box full of pure argon. Galvanostatic charge/discharge tests were performed at the current density of 200 mA g^{-1} with different voltages ranges from 0.01 V to 3 V. cyclic voltammetry (CV) were tested with a scan rate of 0.1 mVs^{-1} and electrochemical impedance spectroscopy (EIS) was tested from 0.01 Hz to 10^5 Hz by a CHI 600A Electrochemical Workstation.

RESULTS AND DISCUSSION

Structural Characterization

The composition and crystallinity of obtained $FeSe_2$ and $FeSe_2$/C composites were investigated by XRD. It can be seen from Fig. 1, the diffraction peaks of samples can be indexed to the orthorhombic phase of $FeSe_2$. The lattice constants of them are that a = 4.810 Å, b = 5.726 Å and c = 3.582 Å, which is in agreement with the standard patterns (JCPDS 65-2570). No other visible impurity peaks are observed, indicating that expected products synthesized by hydrothermal method are pure phase.

Figure 2 represents the different magnification FESEM images of the pure $FeSe_2$ and $FeSe_2$/C composites. As shown in Fig. 2a and b, the images of

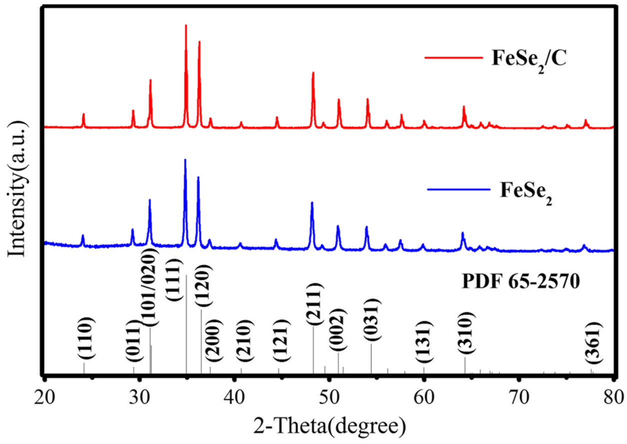

Fig. 1. XRD pattern of pure $FeSe_2$ and $FeSe_2$/C clusters.

$FeSe_2$ displays a 3D structure composed of the tightly stacked and equally distributed nanorods, which had a thickness of 100–300 nm and 0.3–1 μm in length. As shown in Fig. 2c and d, with the carbon composited $FeSe_2$ clusters, the shape of nanorods remains the same, but there are smaller crystal particles occurring around clusters. This shows that in the process of formation composite, the presence of carbon had certain influence on morphologies of products; carbon can hinder the growth of the crystal particles. Hence, the crystal size of nanocubes changed to smaller, and distributed more uniformly. In order to know the distribution and existence of carbon in $FeSe_2$/C composites, the elemental mapping images of Fe, Se, C are shown in Fig. 3, which revealed a uniform distribution of the element Fe and Se over the composite powders and low amorphous carbon content in $FeSe_2$/C composite.

The TEM images of $FeSe_2$ and $FeSe_2$/C were shown in Fig. 4. It can been see from Fig. 4a that $FeSe_2$ was composed by nanorods, the diameter of nanorods have no distinct difference. The bone structure of $FeSe_2$/C in Fig. 4b is the same as $FeSe_2$, meanwhile, there are many small nanoparticles appearring around nanorods. The selected area electron diffraction (SAED) pattern of $FeSe_2$/C was shown in Fig. 4c, which indicates the as-synthesized $FeSe_2$ is single crystal planes. A lattice fringe with ad-spacing of approximately 0.256 nm, which corresponds to the (111) plane of the $FeSe_2$ crystal, is observed in the HRTEM image of Fig. 4d.

TG studied the content of carbon in samples. It can be concluded from Fig. 5, in the temperature range from 25°C to 900°C, the weight loss of $FeSe_2$/C composites is 64.42%. When the temperature is between 200°C and 300°C, with the increase of temperature, the weight increased obviously on account of the formation of SeO_2 and Fe_2O_3 by reaction of the $FeSe_2$ with oxygen in air. When the temperature rises to more than 300°C, it has a very rapid decline curve; the weight lost can be attributed to the amorphous carbon transform into CO_2 and the gasification of SeO_2. The content of C in $FeSe_2$/C composites is about 4.8 wt.%, which was calculated based on followed reaction.

$$4FeSe_2 + 11O_2 \rightarrow 2Fe_2O_3 + 8SeO_2$$

XPS measurements were shown in Fig. 6 to analyze the valence states of $FeSe_2$/C composites. The survey spectrum of $FeSe_2$/C composites in Fig. 6a confirmed the presence of Se, Fe, and C. The main peaks located at 719.94 eV and 707.18 eV (Fig. 6b), corresponding to $Fe2p_{1/2}$ and $Fe2p_{3/2}$ confirm the existence of Fe(II).[19,30] Figure 6c shows

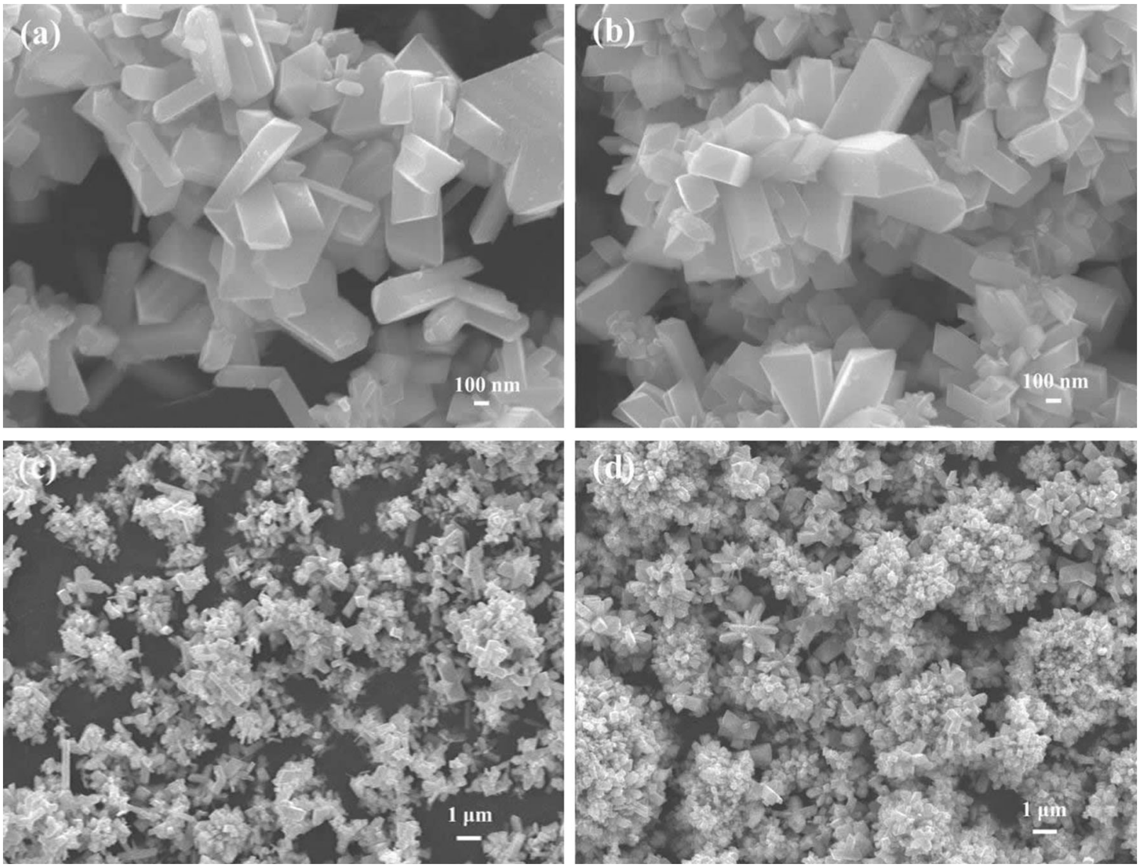

Fig. 2. FESEM images of pure $FeSe_2$ (a, b) and $FeSe_2$/C composites (c, d).

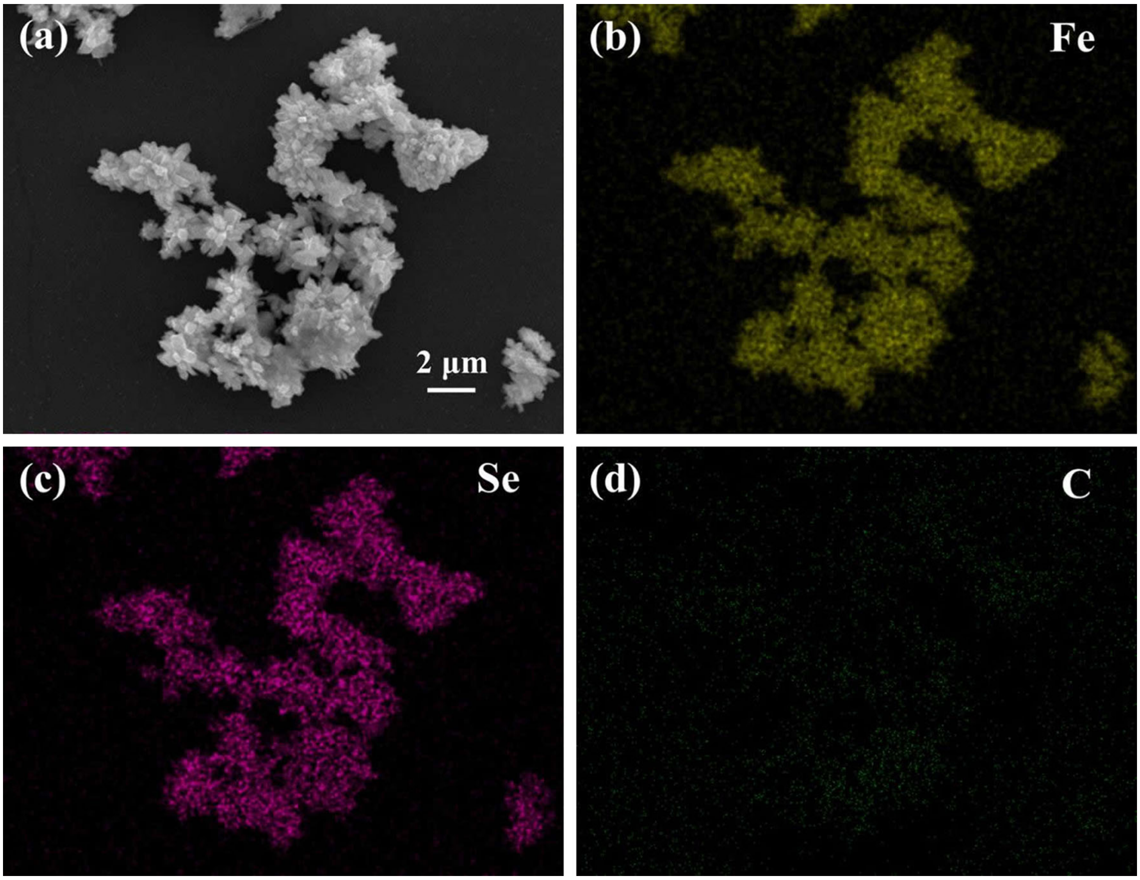

Fig. 3. Elemental mapping images of the as-prepared $FeSe_2$/C clusters.

the 3d peak of the Se element. Two peaks located at 55.31 eV and 54.55 eV, corresponding to Se $3d_{3/2}$ and Se $3d_{5/2}$, which proved further that the expected product was $FeSe_2$.[31] The peak located at 284.8 eV in Fig. 6d corresponds to the binding energy of the sp^2 C–C bond,[32,33] it illustrates that glucose was formed into amorphous carbon during a hydrothermal process.

Electrochemical Properties

The electrochemical properties of raw $FeSe_2$ and $FeSe_2$/C composites were tested by assembling into lithium ion batteries. The initial five cycles CV curves in the range of 0.01–3.0 V at 0.1 mV s^{-1} are shown in Fig. 7a. As we can see, there are two reduction peaks appearing at 1.44/0.71 V and two oxidation peaks at 1.96/2.28 V observed in the first CV curve. The peak at 1.44 V corresponding to insertion of Li ions into $FeSe_2$ nanocubes ($FeSe_2 + 4Li^+ + 4e^- \rightarrow Fe + 2Li_2Se$), the peak around 0.71 V implied the irreversible formation of SEI film.[34] Meanwhile, the peak around 1.96 V may be attributed to the formation of $Li_{2-x}FeSe_2$, which includes the two reactions:

$$Fe + 2Li_2Se \rightarrow Li_2FeSe_2 + 2Li^+ + 2e^-$$

$$Li_2FeSe_2 \rightarrow Li_{2-x}FeSe_2 + xLi^+ + xe^-$$

The peak at 2.28 V resulted from the generation of $FeSe_y$ and Se. In the following four cycles, two reduction peaks at 1.93 V and 1.44 V, are related to these two reactions:

$$FeSe_y + (2-y)Se + 2Li^+ + 2e^- \leftrightarrow Li_2FeSe_2 (1.93\ V)$$

$$Li_2FeSe_2 + 2Li^+ + 2e^- \leftrightarrow Fe + 2Li_2Se\ (1.44\ V)$$

As can be seen from the CV curves, the first curve is not the same as the following curves, which illustrates that there is an irreversible reaction happening in the first cycle. In these five cycles, the oxidation/reduction peaks still occur in the same place. However, the peak area of the first three cycles is decreasing, and the four and five cycles have the almost same peak area which indicates the discharge capacity have a stable tendency in subsequent cycles.

Figure 7b displays the first three charge/discharge curves at 200 mA g^{-1} from 0.01 V to 3 V, the potential plateaus in charge/discharge process match well with the CV curves. The first charge and discharge capacities of $FeSe_2$/C composites are 1160 mA h g^{-1} and 1725 mA h g^{-1} with the capacity retention of 70.6%. The capacity fading during the first cycle is irreversible, which can be attributed to the formation of SEI film, electrolyte decomposition

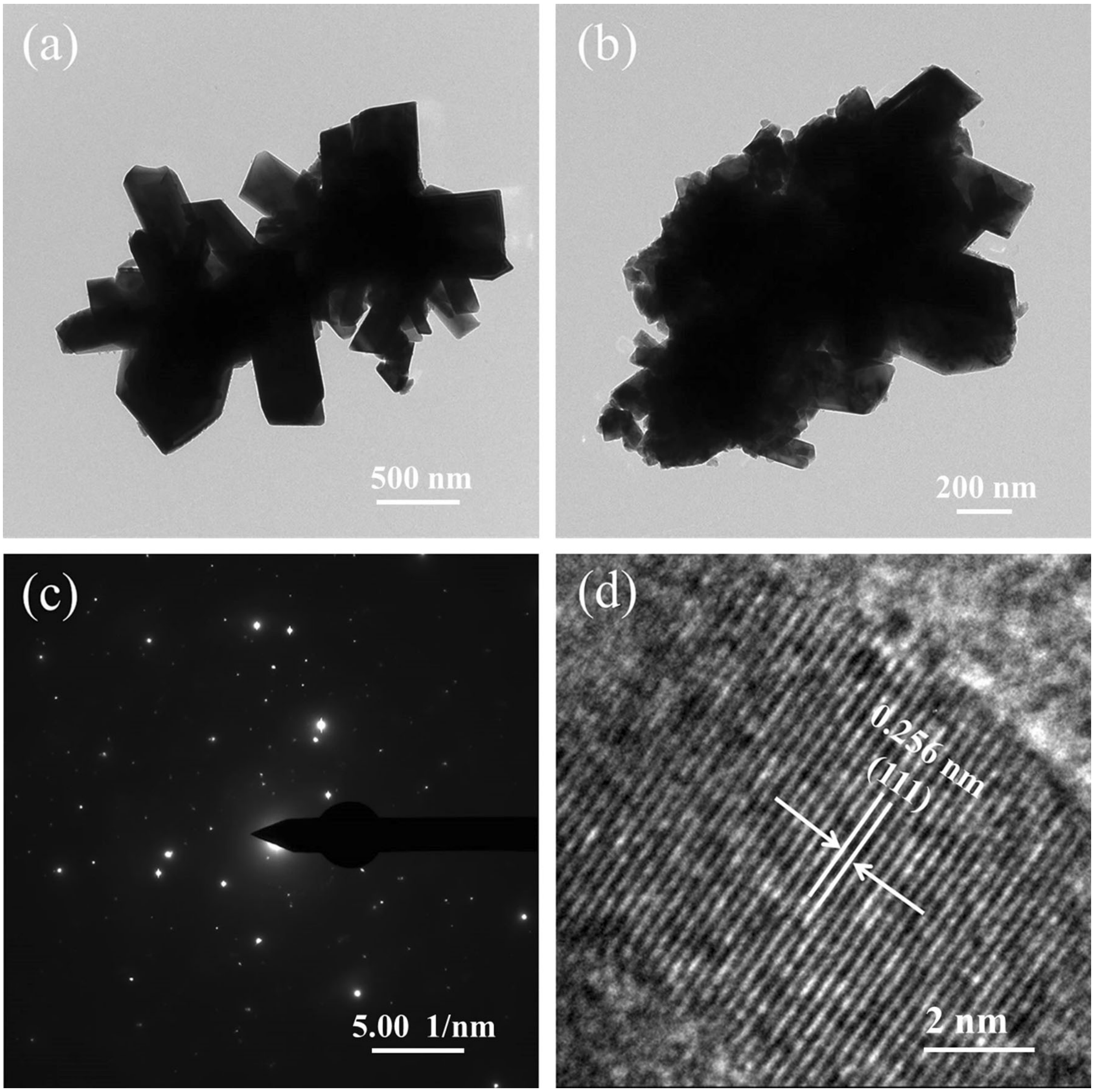

Fig. 4. (a) TEM image of pure $FeSe_2$; (b) TEM image of $FeSe_2$/C composites; (c) SAED pattern of $FeSe_2$/C composites; (d) HRTEM image of $FeSe_2$/C.

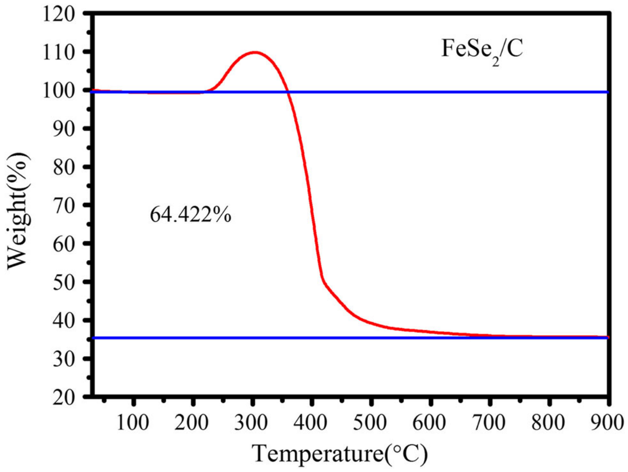

Fig. 5. TG curves of $FeSe_2$/C composites.

and inadequate decomposition of Li_2Se. In subsequent two cycles, the discharge specific capacity of 1217 mA h g^{-1} and 1167 mA h g^{-1} are obtained with high capacity retention rates of 90% and 95%, indicating the $FeSe_2$/C composites have good reversible specific capacity and remarkable cycling stability.

Figure 7c represents the cycling performance comparison of $FeSe_2$ and $FeSe_2$/C at 200 mA g^{-1}. It is clear that the $FeSe_2$/C electrode behaves in a higher reversible capacity than that of pure $FeSe_2$. The discharge capacity of $FeSe_2$ was 725 mA h g^{-1} after 100 cycles. Meanwhile, the discharge capacity of $FeSe_2$/C electrode reaches to 1060 mA h $g^{-1}$and the capacity retention after the first cycle is nearly 100%. In the process of discharge, there is a trend showing the specific capacity increase of $FeSe_2$/C in the initial 30 cycles, which can be mainly attributed

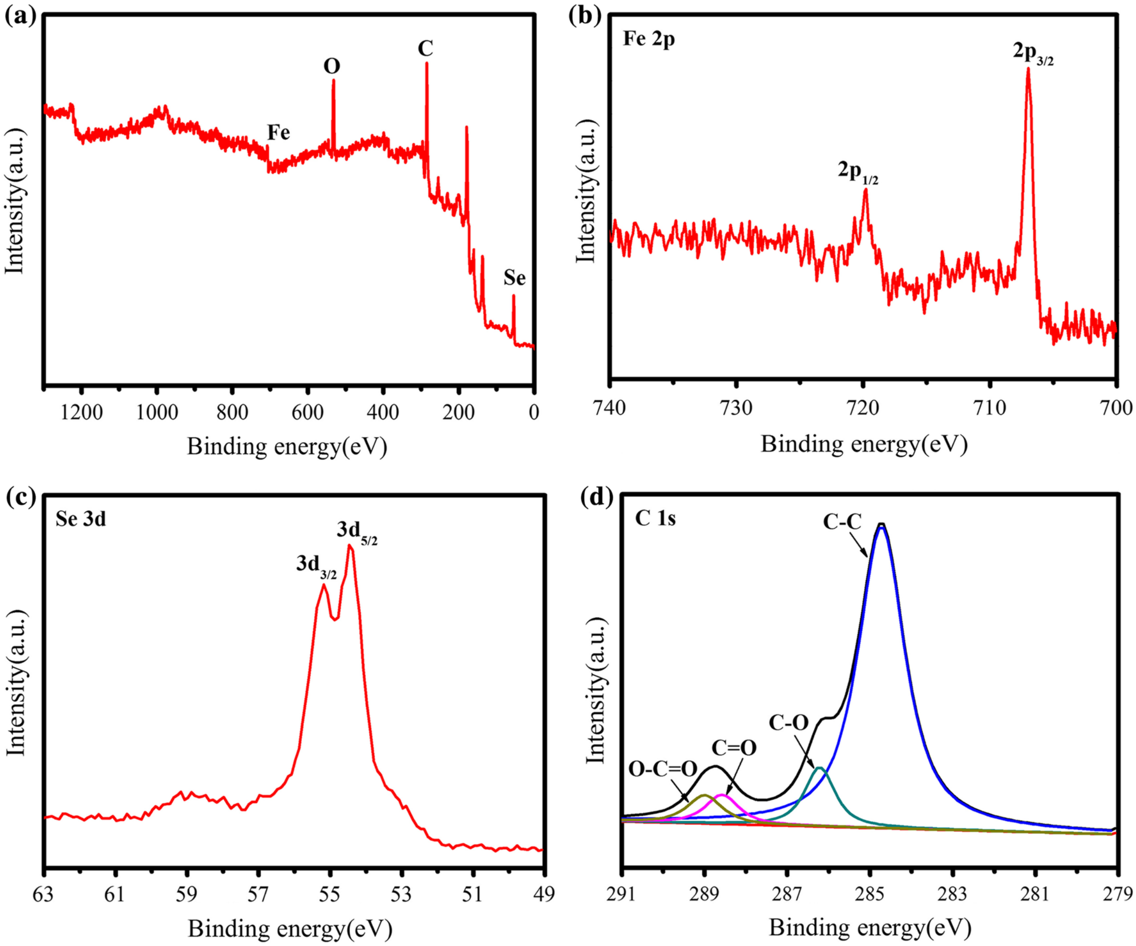

Fig. 6. XPS spectra of $FeSe_2$/C composites: (a) Wide-scan XPS spectrum; (b) Fe 2p; (c) Se 3d; (d) C 1s.

to an activation process with full infiltration by the electrolyte.[35] The rate performance of the $FeSe_2$/C and $FeSe_2$ were shown in Fig. 7d. The $FeSe_2$/C electrode delivers a discharge capacity of 1140 mA h g^{-1}, 1090 mA h g^{-1}, 1008 mA h g^{-1}, 850 mA h g^{-1}, 697 mA h g^{-1} and 470 mA h g^{-1} at different current rates from 0.2 A g^{-1}, 0.4 A g^{-1}, 1 A g^{-1}, 2 A g^{-1} to 5 A g^{-1}. When the current density returned to 0.2 A g^{-1} after 60 cycles, the reversible capacity could also be able to return to 1183 mA h g^{-1}, and means outstanding Li^+ storage reversibility. The capacities for raw $FeSe_2$ are 737 mA h g^{-1} at 0.2 A g^{-1} and only 325 mA h g^{-1} can be retained at 5 A g^{-1}. The remarkable electrochemical property of the $FeSe_2$/C electrode may be interpreted as the presence of carbon which improved the conductivity of the $FeSe_2$/C material and increase electron transportation in the electrode materials, meanwhile, it reduce the size of the nanocubes and prevented the aggregation of nanocubes during the discharge/charge process.

Figure 8a shows the EIS of the $FeSe_2$/C composites and $FeSe_2$. It is obvious that the EIS curve is made up of one semicircle and one straight line. The existence of the high frequency semicircle can be interpreted as the formation of a SEI layer and contact resistance, while the medium frequency region is concerned with the charge transfer resistance on the electrolyte–electrode interface, and the low frequency line is assigned to the diffusion effect of Li-ion. The equivalent circuit can be utilized to simulate the charge–discharge processes and is revealed with EIS curves, which is used for the impedance data analysis, shown in Fig. 8a. Typically, Rs stands for the electrolyte resistance in accord with intercept of the semicircle, Rct and Cdl are referred to as the charge-transfer resistance and related double-layer capacitor, Zw is Warburg impedance in accord with the diffusion of lithium ions. It can be observed that the semicircle diameter of $FeSe_2$/C is smaller than $FeSe_2$. This suggests that the $FeSe_2$/C electrode possesses lower charge-transfer and contact impedance. The linear fitting of the Warburg impedance is shown in Fig. 8b, the Warburg coefficient (Aw) is obtained by calculating the slope of the Z' versus$\omega^{-1/2}$ line at low frequency. The values of Li^+ diffusion coefficient can be estimated from the equation[36]:

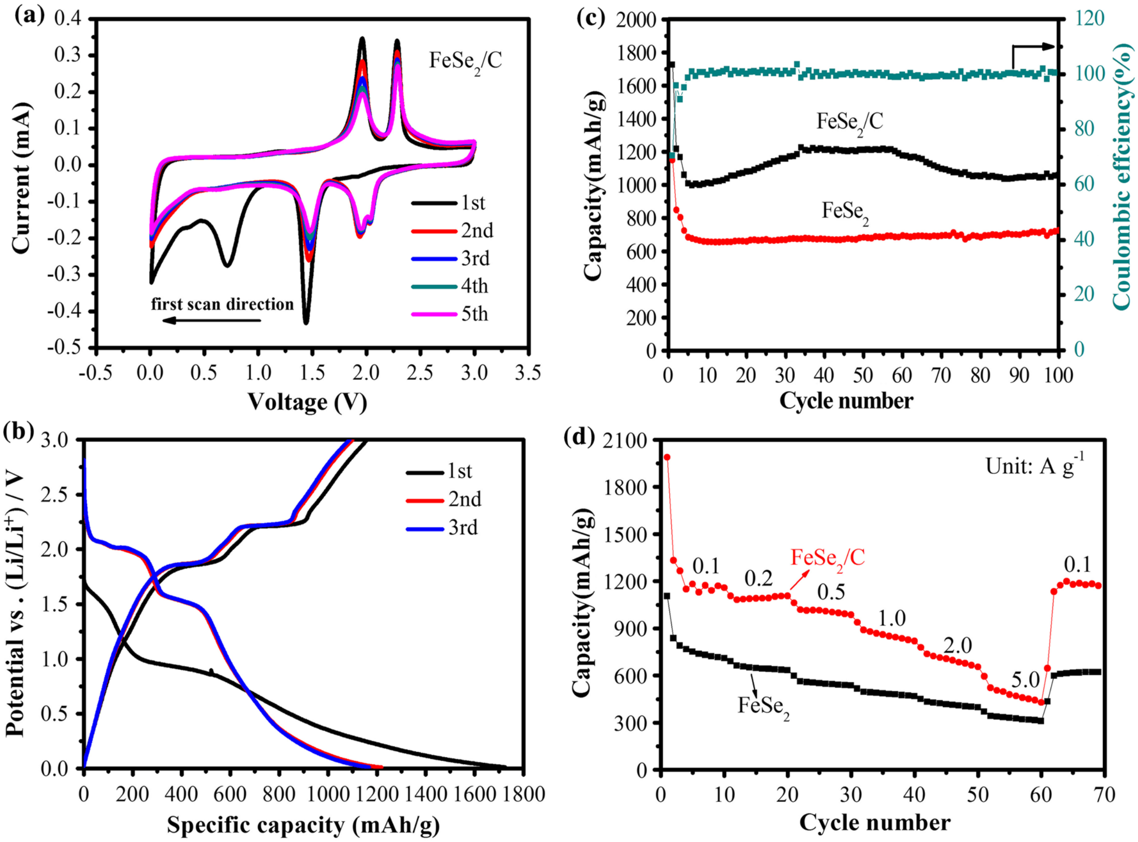

Fig. 7. (a) CV curves; (b) charge/discharge voltage profiles of $FeSe_2/C$ composites; (c) cycling performance of $FeSe_2$ and $FeSe_2/C$ at 200 mA g^{-1} for 100 cycles as well as the corresponding coulombic efficiency of $FeSe_2/C$; (d) rate performance of $FeSe_2$ and $FeSe_2/C$.

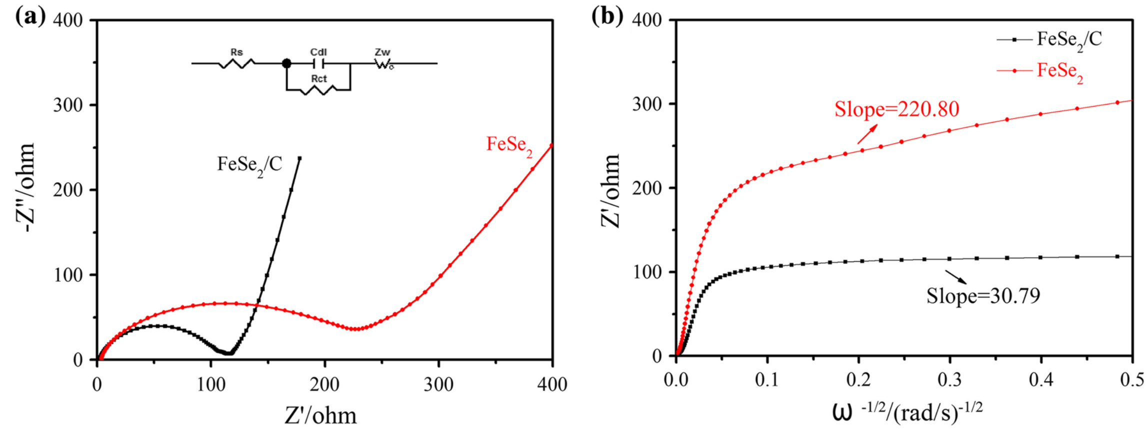

Fig. 8. (a) Electrochemical impedance spectra of pure $FeSe_2$ and $FeSe_2/C$ composites; (b) linear fitting of Warburg impedance of pure $FeSe_2$ and $FeSe_2/C$ composites.

$$D_{\mathrm{Li}^+} = 0.5\left[\frac{\mathrm{V}_m}{FSA_w}\left(-\frac{\mathrm{d}E}{\mathrm{d}x}\right)\right]^2.$$

The V_m, F, S and $(-\mathrm{d}E/\mathrm{d}x)$ appearing in the above are constants for the model test cells, which accord with molar volume, Faraday constant, surface area of electrode and the slope of the open-circuit potential versus the mobile ion concentration x at each x value, respectively. Hence, the D^+_{Li} is directly proportion to $(1/A_w)^2$. It is obvious that the Warburg coefficient A_w of $FeSe_2/C$ is smaller than $FeSe_2$, which indicates that the ionic conductivity of $FeSe_2/C$ is better than $FeSe_2$. These results also confirm that the electric conductivity is greatly increased and electron/ion transfer faster in $FeSe_2/C$ due to the existence of carbon.

CONCLUSIONS

In summary, the $FeSe_2$/C clusters were successfully synthesized by an ordinary hydrothermal method. The as-synthesized $FeSe_2$/C composites were used as anode material and fabricated into LIBs, and exhibited preferable lithium storage performance, such as a higher specific discharge capacity, better cycling stability and superior rate capability compared with pure $FeSe_2$. The excellent electrochemical performance of $FeSe_2$/C composites is ascribed to the unique 3D structure and the existence of amorphous carbon in the $FeSe_2$/C composites. Typically, the carbon in $FeSe_2$/C composites can act as the conductive matrix that dramatically improves the electric conductivity and accelerates electron transportation in the electrode materials. Furthermore, carbon also maintains structural integrity of the material and hinders the aggregation of nanocubes. The $FeSe_2$/C composites have more uniform distribution, led to a higher surface area, which provides a large effective area for a better contact between the active materials and electrolyte. Therefore, the $FeSe_2$/C composites may be a promising anode material for LIBs application.

REFERENCES

1. F. Un-Noor, S. Padmanaban, L. Mihet-Popa, M. Mollah, and E. Hossain, *Energies* 10, 1217 (2017).
2. T. Wilberforce, Z. El-Hassan, F.N. Khatib, A. AlMakky, A. Baroutaji, J.G. Carton, and A.G. Olabi, *Int. J. Hydrogen. Energ.* 42, 25695 (2017).
3. Z. Omariba, L. Zhang, and D. Sun, *Electronics* 7, 72 (2018).
4. N. Nitta, F. Wu, J.T. Lee, and G. Yushin, *Mater. Today* 18, 252 (2015).
5. G. Zhu, L. Wang, H. Lin, L. Ma, P. Zhao, Y. Hu, and J. Liu, *Adv. Funct. Mater.* 28, 1800003 (2018).
6. C.L. Tan and H. Zhang, *Chem. Soc. Rev.* 44, 2713 (2015).
7. X.S. Zhou, X. Zhou, L.J. Wan, and Y.G. Guo, *Chem. Commun.* 49, 1838 (2013).
8. Q.F. Wang, R. Zou, W. Xia, J. Ma, B. Qiu, A. Mahmood, and Q. Xu, *Small* 11, 2511 (2015).
9. L. Xu, Y. Hu, H. Zhang, H. Jiang, and C. Li, *ACS Sustain. Chem. Eng.* 4, 4251 (2016).
10. Z.A. Zhang, X. Shi, X. Yang, Y. Fu, K. Zhang, Y. Lai, and J. Li, *ACS Appl. Mater. Interfaces* 8, 13849 (2016).
11. T. Li, A. Qin, L. Yang, J. Chen, Q. Wang, D. Zhang, and H. Yang, *A.CS Appl Mater. Interfaces* 9, 19900 (2017).
12. S.S. Huang, Q. He, W. Chen, Q. Qiao, J. Zai, and X. Qian, *Chem. Eur. J.* 21, 4085 (2015).
13. K. Zhang, Z. Hu, X. Liu, Z. Tao, and J. Chen, *Adv. Mater.* 27, 3305 (2015).
14. W.J. Wang, X. Pan, W. Liu, B. Zhang, H. Chen, X. Fang, and S. Dai, *Chem. Commun.* 50, 2618 (2014).
15. W.D. Shi, X. Zhang, G. Che, W. Fan, and C. Liu, *Chem. Eng. J.* 215, 508 (2013).
16. A. Sobhania and M. Salavati-Niasari, *J. Alloys. Compd.* 625, 26 (2015).
17. X.J. Wei, C. Tang, Q. An, M. Yan, X. Wang, P. Hu, and L. Mai, *Nano Res.* 10, 3202 (2017).
18. X. Chang, J. Jian, G. Cai, R. Wu, and J. Li, *Electron Mater. Lett.* 12, 237 (2016).
19. J. Xu, K. Jang, J. Lee, H.J. Kim, J. Jeong, J.G. Park, and S.U. Son, *Cryst. Growth Des.* 11, 2707 (2011).
20. B. Yuan, W. Luan, and S.T. Tu, *Dalton. Trans.* 41, 772 (2012).
21. A.Q. Pan, H.B. Wu, L. Yu, and X.W. Lou, *Angew. Chem.* 125, 2282 (2013).
22. C.J. Niu, J. Meng, C. Han, K. Zhao, M. Yan, and L. Mai, *Nano Lett.* 14, 2873 (2014).
23. C. Yang, H. Zhao, Y. Hou, and D. Ma, *J. Am. Chem. Soc.* 134, 15814 (2012).
24. J.P. Yang, D. Shen, L. Zhou, W. Li, X. Li, C. Yao, and D. Zhao, *Chem. Mater.* 25, 3030 (2013).
25. M.Y. Ge, Y. Lu, P. Ercius, J. Rong, X. Fang, M. Mecklenburg, and C. Zhou, *Nano Lett.* 14, 261 (2014).
26. Y. Zhu, X. Fan, L. Suo, C. Luo, T. Gao, and C. Wang, *ACS Nano* 10, 1529 (2016).
27. J. Liu, Y. Wen, Y. Wang, P.A. van Aken, J. Maier, and Y. Yu, *Adv. Mater.* 26, 6025 (2014).
28. J.C. Guo, Q. Liu, C. Wang, and M.R. Zachariah, *Adv. Funct. Mater.* 22, 803 (2012).
29. Q. Su, X. Cao, X. Kong, Y. Wang, C. Peng, J. Chenand, and A. Pan, *Electrochim. Acta* 292, 339 (2018).
30. G.D. Park, J.H. Kim, and Y.C. Kang, *Mater. Charact.* 120, 349 (2016).
31. Q.L. Zheng, Q. Zheng, X. Cheng, and H. Li, *Catalyst* 5, 1079 (2015).
32. L.M. Wang, B. Liu, S. Ran, H. Huang, X. Wang, B. Liang, and G. Shen, *J. Mater. Chem.* 22, 23541 (2012).
33. C.C. Li, X. Yin, L. Chen, Q. Li, and T. Wang, *Chem. Eur. J.* 16, 5215 (2010).
34. B.H. Qu, C. Ma, G. Ji, C. Xu, J. Xu, Y.S. Meng, and J.Y. Lee, *Adv. Mater.* 26, 3854 (2014).
35. J. Luo, J. Liu, Z. Zeng, C.F. Ng, L. Ma, H. Zhang, and H.J. Fan, *Nano Lett.* 13, 6136 (2013).
36. W. Wang, Y. Yang, S. Yang, Z. Guo, C. Feng, and X. Tang, *Electrochim. Acta* 155, 29 (2015).